High cycle fatigue life estimation of materials processed by laser powder bed fusion

Authors: Even W. Hovig[1*], Amin S. Azar[2], Martin F. Sunding[2], Erik Andreassen[2], Knut Sørby[1]

[1]Norwegian University of Science and Technology, Trondheim, Norway

[2]SINTEF Industry, Oslo, Norway

[*]Corresponding author: even.w.hovig@ntnu.no

Abstract

The fatigue life of metal components is known to depend on the surface topography. For components made by laser powder bed fusion, the roughness of the as-built surfaces depends on the orientation of the component surface with respect to the build plate. Surface topographies of AlSi10Mg and Inconel 718 specimens built at 0° to 90° inclination, with 15° increments, were characterised by white light interferometry. Two methods for calculating the stress concentration factor using the surface roughness data are proposed and the results of each approach are presented and compared. Moreover, a finite element model was developed, in order to analyse the stress field when subsurface porosity is present. The fatigue lifetime estimates suggest that the lifetime of components may differ up to two orders of magnitude, depending on the build orientation.

Keywords

Additive Manufacturing, Powder Bed Fusion, Laser Melting, Stress Concentration Factor, Fatigue, Inconel 718, AlSi10Mg

Nomenclature

d	Distance from main surface down to the tip of a defect (e.g. crack or groove)
h	Laser scanning hatch spacing
k_t	Stress concentration factor
L	Peak to peak distance of a surface profile
N_f	Number of fatigue cycles to failure
P	Laser power
R	Min-to-max stress ratio in fatigue test
R_a	Arithmetical mean deviation of surface profile
R_{da}	Average absolute slope of the surface profile within the sampling length
R_v	Maximum valley depth of a surface profile in the evaluation length
R_{vm}	Average maximum valley depth of surface profile of each sample length within an evaluation length
R_z	Average distance between the highest peak and lowest valley of a surface profile
S	Mean spacing between adjacent local peaks of a surface profile
t	Layer thickness used in the powder bed fusion process
T_s	Substrate temperature
v	Laser scan velocity
σ	Stress amplitude
σ_{max}	Maximum local stress
σ_{nom}	Nominal global stress
ρ	Radius at tip of defect
ν	Poisson's ratio

1. Introduction

Additive manufacturing (AM) is a process where material is added, typically layer by layer, to form a three-dimensional part. The most common AM process for metals is laser metal powder bed fusion (LPBF), in which a layer of the feedstock material, typically a pre-alloyed powder, is distributed over a substrate, and then the layer is selectively melted by a laser to build a certain geometry and fuse with the previous layer. A number of materials and alloys for LPBF are commercially available, and process parameters have been optimised for each machine type and material system[1]. In this study, one aluminium alloy and one iron-nickel based superalloy are considered. AlSi10Mg is typically used in casting of parts with complex geometry and thin walls, e.g. automotive applications. Inconel 718 is a high temperature alloy that is typically used in aerospace where excellent mechanical properties at elevated temperatures is critical. Additive manufacturing of these alloys allows for complex geometries, but there are some issues compared to their cast or wrought counterparts, such as higher surface roughness, different microstructures, higher porosity etc. Therefore, specific knowledge of AM material performance is of great importance for demanding applications such as automotive and aerospace.

The fatigue life of AM components is affected by several features; component size, surface characteristics, internal porosity, sub-surface porosity and microstructure. Predicting the fatigue life of a component with defects requires appropriate definition of stress concentration factors (SCF). We can distinguish between the SCFs of the nominal geometry and those of process-induced defects (defects at the surface or in the bulk of the component). The stress concentration factor is defined as:

$$k_t = \sigma_{max}/\sigma_{nom} \tag{1}$$

where k_t is the SCF, σ_{max} is the maximum stress in the component and σ_{nom} is the externally applied stress. For a U-shaped surface defect under uniaxial loading, the SCF can be estimated according to equation (2),

$$k_t = 1 + 2\sqrt{\frac{d}{\rho}} \tag{2}$$

where d is the distance from the surface to the tip of the defect, and ρ is the radius at the tip[2]. Depending on the cumulative stress concentration, based on the type and size of defects in the component, either internal or surface defects will play a dominant role. Internal defects can be characterized by non-destructive methods (e.g. X-ray micro-computed tomography (μ-

CT)[3]) or destructive methods (e.g. microscopy of cross-sections etc.), while surface defects are usually characterized by microscopy or interferometry.

There are several studies on estimating the fatigue life of AM components based on internal and external defects[4-8]. Romano et al.[4,5] proposed a model based on internal defects to predict both low-cycle and high-cycle fatigue in AlSi10Mg, based on assumptions regarding defect size, geometry, and occurrence. Yadollahi et al.[6] applied a similar method to describe the effect of surface texture and defect features on the fatigue life of Inconel 718. The latter article suggested using the maximum valley depth of the surface profile (R_v) as the initial crack length for fatigue life modelling. However, this approach does not account for the geometry of the defect. Yamashita et al.[7] studied the effect of internal defects on fatigue life of Inconel 718. They concluded that the area of a defect must be seen in relation with other defects in the immediate proximity, and expanded the model to give a more accurate prediction. Zhou et al.[8] investigated the effect of texture on low-cycle fatigue of Inconel 718. Along with other studies on the microstructure of LPBF Inconel 718[9-11], they found that the as-built microstructure consists of a predominantly columnar grain structure parallel to the build direction. This structure will result in an anisotropic mechanical response, making the fatigue life dependent on build orientation in addition to internal and external defects.

The models mentioned in the previous paragraph use internal defect geometry as input to estimate the fatigue life. In an effort to eliminate the need for destructive testing such as microscopy, or high-cost equipment such as μ-CT to characterize internal defects, this paper propose models based on only surface roughness measurements. However, if sub-surface porosity is present, internal defects must be accounted for, as will be demonstrated in section **Feil! Fant ikke referansekilden.**.

Several experimental studies on the fatigue life of AlSi10Mg alloys with respect to different LPBF processing parameters have been conducted in the recent years[12-16]. Among the findings, the key conclusions suggest that elevating the substrate temperature during LPBF processing, and post-LPBF heat treatment (T6) of the as-built samples, increase the fatigue life significantly. The microstructure will recrystallize upon solution heat treatment, which in turn will mitigate the anisotropic effect of the as-built columnar microstructure. A more comprehensive summary of the experimental studies is available in Hovig et al.[17]. Furthermore, machining and shot-peening of the surfaces increase the lifetime compared to the as-built performance. Bagherifard et al.[18] demonstrates how sand blasting and shot

peening can significantly increase the fatigue strength of AlSi10Mg LPBF specimens, and Beevers et al.[19] investigated the effect of various processing parameters and post treatments. The latter study showed that LPBF processing without contour scan, and post processing with vibration polishing, increased the fatigue life of net-shape specimens to the level of machined specimens.

There have also been several experimental studies on the fatigue life of LPBF Inconel 718. Scott-Emuakpor et al.[20] reported fatigue life of polished samples built in parallel with the LPBF build direction before and after hot isostatic pressing (HIP) treatment. The results indicate that HIP marginally increases the fatigue lifetime for high fatigue loads, while no apparent difference is seen in low fatigue loads (high cycle fatigue). Kelley et al.[21] reported fatigue life of Inconel 718 based on orientation for both machined and rough samples built both parallel and perpendicular to the build direction and demonstrates that the fatigue life drastically decreases when no surface treatment is done post LPBF processing. Konečná et al.[22] reported fatigue life of three sets of rough surface aged samples built in three different orientations. The study shows how surface roughness and orientation influences the fatigue life, where the smoothest surfaces yielded the highest fatigue life also for aged samples. Balachandramurthi et al.[23] demonstrated how the fatigue life of samples built in parallel to the build direction responds to heat treatments and surface machining for both electron beam melting and LPBF. It was shown that HIP treatment followed by ageing and surface machining improved the fatigue life of the components significantly.

As for AlSi10Mg, ageing Inconel 718 increases the low cycle fatigue life compared to only surface machining. Nevertheless, machining the surface still significantly increases the fatigue life, especially at low stress levels (high cycle fatigue). When comparing the fatigue life data from the literature it becomes apparent that the machine-to-machine repeatability is low. The fatigue life of the same alloy built by different vendors does not have comparable tensile properties, surface roughness, and consequently fatigue lives.

Having established the significance of surface roughness on the high cycle fatigue life for both AlSi10Mg and Inconel 718, it becomes critical to account for surface roughness when designing LPBF components. In order to capitalize on the design freedom offered by LPBF, surface machining is often impractical, or even impossible. In this study, we propose two approaches for determining the stress concentration factors due to process-induced roughness, for flat surfaces of specimens made by LPBF. One approach uses white light

interferometry to characterize the surface roughness, while the other approach utilizes a stylus-type measurement for surface roughness characterization.

2. Materials and methods

The AlSi10Mg specimen were fabricated with a Concept Laser M2 Cusing machine. The powder feedstock was supplied by GE Additive (CL31AL). The processing parameters for AlSi10Mg were developed by optimizing the relative density of the material. The Inconel 718 specimens were built with an SLM 280 HL machine with process parameters for Inconel 718 powder as supplied by the machine manufacturer. The nominal chemical compositions of the AlSi10Mg and Inconel 718 alloys can be seen in Table 1 and Table 2, respectively. The main processing parameters are listed in Table 3.

Table 1 Chemical composition of the AlSi10Mg powder feedstock as given by the supplier.

Element	**Si**	**Mg**	**Fe**	**Mn**	**Ti**	**Cu**	**Zn**	**C**	**Al**
wt%	9.0-11.0	0.2-0.45	<0.55	<0.45	<0.15	<0.1	<0.1	<0.05	bal.

Table 2 Chemical composition of the Inconel 718 powder feedstock as given by the supplier.

Element	**Ni**	**Cr**	**Al**	**Mo**	**Nb (+Ta)**	**Ti**	**Fe**
wt%	50-55	17-21	0.2-0.8	2.8-3.3	4.75-5.5	0.6-1.1	bal.

Table 3 Main processing parameters for LPBF of AlSi10Mg and Inconel 718 used in this study.

Material	**Layer thickness [t]**	**Hatch spacing, [h]**	**Laser power, [P]**	**Scan velocity, [v]**	**Substrate temperature, [T_s]**
AlSi10Mg	30 µm	97.5 µm	200 W	1200 mm/s	200°C
Inconel 718	50 µm	120 µm	250 W	805 mm/s	25°C

The fabricated parts were miniature flat tensile test specimens (length 45 mm, width in the reduced area section 2.5 mm, thickness 1.5 mm) as shown as inset in Fig. 1. The specimens made from AlSi10Mg were processed with the island scan strategy (island size of 5 × 5 mm^2, X and Y shift of 1 mm, and angular shift of 45°). One additional contour scan was used, on the inside of the specimen surface perimeter. Each layer was first scanned with a low laser power of 50 W to dry and preheat the powder. Argon gas was used to shield the build chamber. The specimens made from Inconel 718 were produced according to the machine manufacturers' specification.

For both materials, specimens with seven different build orientations were selected for surface topography characterization by white light interferometry (WLI) using a Wyko NT-9800 instrument.

Table 4 shows the selected specimens with annotation according to ISO/ASTM 52921:2013E.

Table 4 Specimen annotation according to ISO/ASTM 52921:2013E

Specimen #	**1**	**2**	**3**	**4**	**5**	**6**	**7**
Designation	XY	XY+15B	XY+30B	XY+45B	XY+60B	XY+75B	ZY

The AlSi10Mg specimens were first solution annealed at 538°C followed by and artificial ageing at 160°C for 12 hours (T6). Both sets of the Inconel 718 specimens received solution treatment, and one set was HIPed and aged. The heat treatment procedure for the Inconel 718 specimens can be found in Hovig et al.[24].

The upward facing as-built surfaces were characterized by WLI and analysed in the Veeco Vision 4.2 software. Two areas of 1.7×2.3 mm^2 were captured in the reduced-area region of each of the specimens. The raw data was filtered with a long wavelength pass Gaussian filter and spatial cut-off of 20 μm. Initial investigation revealed that partially melted powder particles were fused to the surface; therefore, the upper 'tail' of the distribution of the surface height was masked for the SCF estimation. Further analysis of the filtered topography was carried out with in-house Matlab scripts.

3. Results and discussion

3.1. Roughness measurements

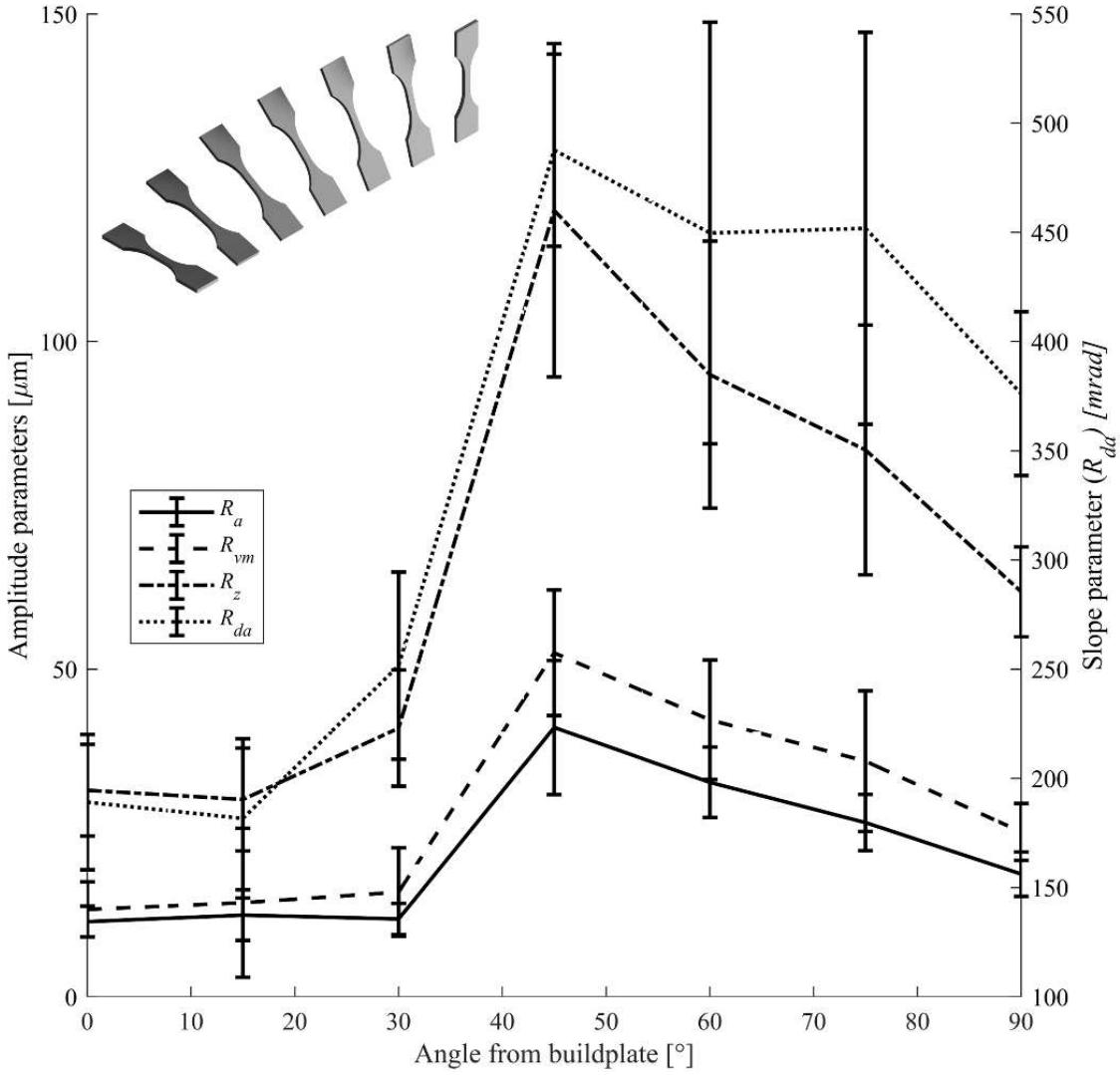

Fig. 1 Selected WLI roughness measurements for the AlSi10Mg specimens (oriented from 0° (XY) to 90° (ZY) with 15° increments). The inset shows the orientations of each specimen from 0° to 90°. The error bars indicate the standard deviation of the measurement within each measured area.

Fig. 1 shows selected surface roughness measurements for the AlSi10Mg specimens, as captured by WLI. The arithmetic mean deviation of the roughness profile (R_a) is at the lowest for the samples oriented at 0°, 15°, and 30°, before a steep increase in surface roughness at 45°, followed by a decline in surface roughness as the samples are 'raised' to 90° inclination. The average depth of the valleys (R_{vm}), the average distance between the peaks and the valleys (R_z), and the average absolute slope measured in radians (R_{da}) all follow the same trend as the arithmetical mean deviation (R_a). Fig. 2 and Fig. 3 show the same roughness parameters for the Inconel 718 specimens, in the as-built and HIP + ageing heat treatment conditions, respectively.

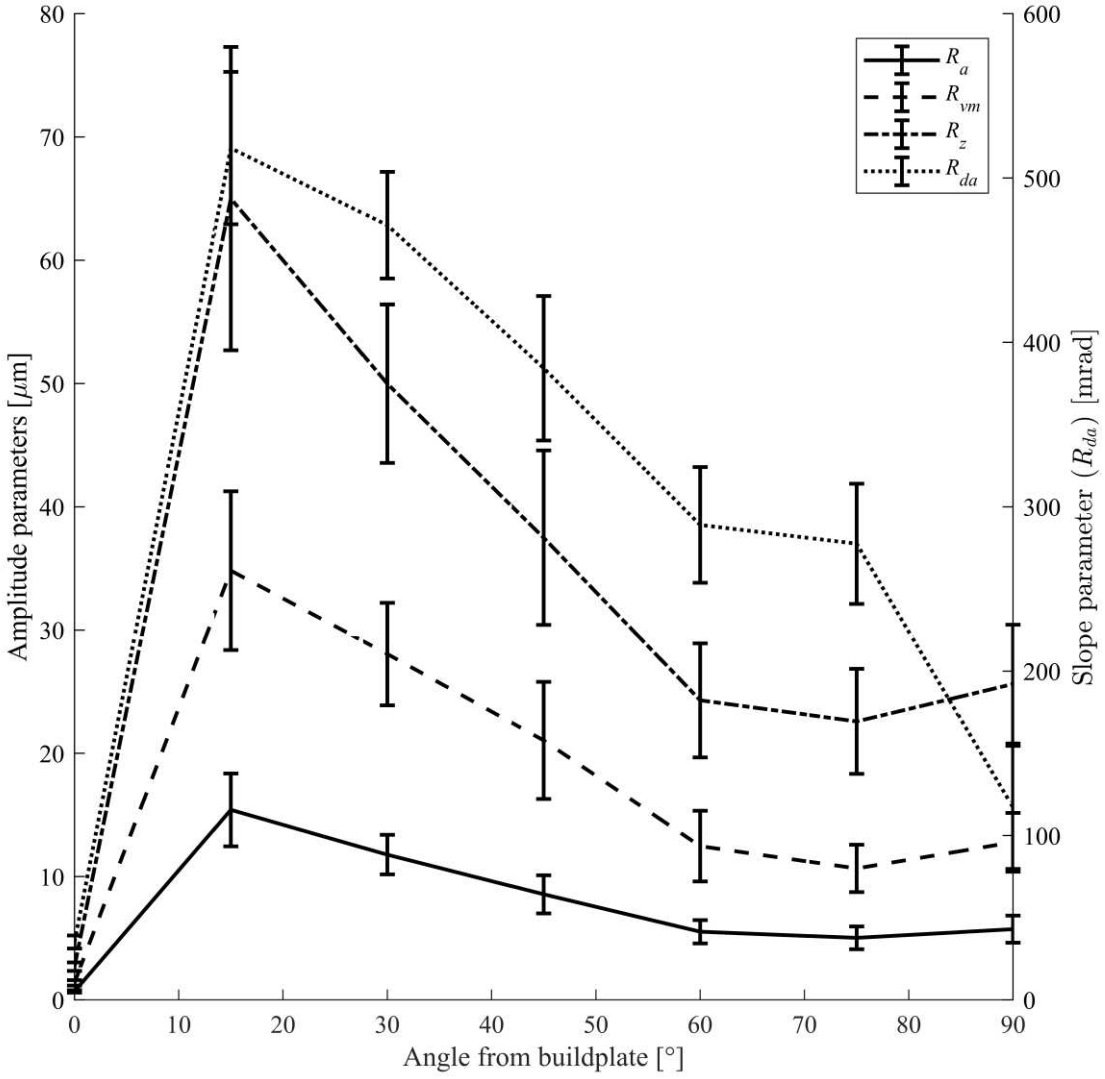

Fig. 2 Selected roughness measurements for the as-built Inconel 718 specimens (oriented from 0° to 90° with 15° increments).

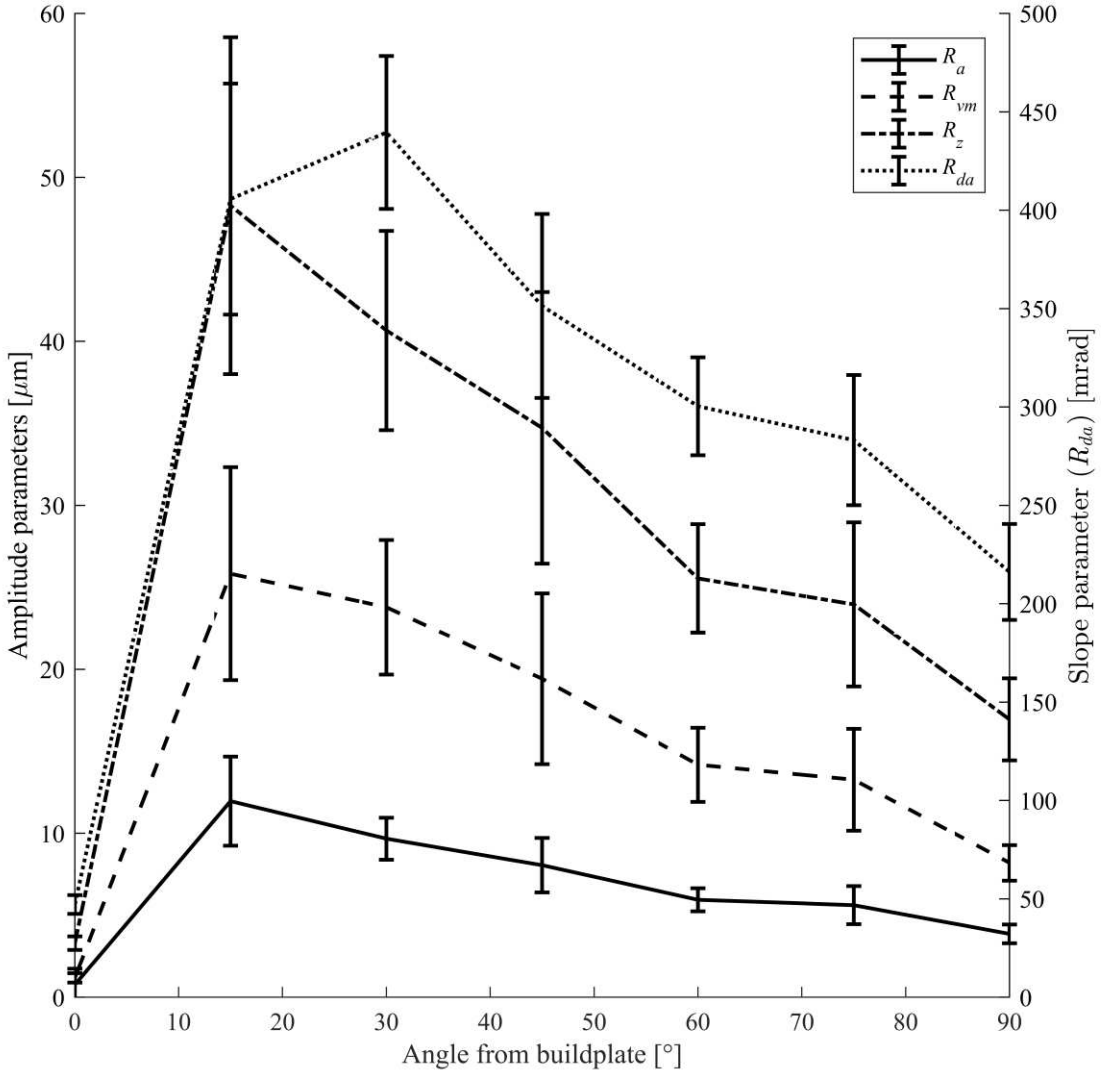

Fig. 3 Selected roughness measurements for the HIP + aged Inconel 718 specimens (oriented from 0° to 90° with 15° increments).

Our roughness data for the AlSi10Mg (Fig. 1) specimens does not match the LPBF roughness data reported by Boschetto et al.[25] for AlSi10Mg, and by Strano et al. for stainless steel[26], as well as our data of Inconel 718, in which the peak in roughness appears at lower angles. As a result, the surface roughness profile of the AlSi10Mg specimens (Fig. 1) fits poorly with the surface roughness model introduced by Boschetto et al. Several factors will determine the final surface roughness during specimen fabrication, such as powder particle size and morphology, layer height, and process parameters.

The surface roughness vs. build angle for the Inconel 718 specimens follows the trends reported by other authors for AM materials[25,26]; the surface roughness is lowest for the

horizontal specimen (0°), followed by a peak in roughness at 15°, and then a decline as the specimens are 'raised' towards the vertical orientation (90°). For the 15° and 30° specimens, the surface roughness values of HIP plus aged Inconel 718 are lower than those of the as-built specimens. It appears that the highest features of the surface are knocked down in the HIP process. The major difference in scan strategy between the AlSi10Mg and Inconel 718 specimens is that the island scan strategy was used for the former material.

As can be seen in the variation of the results from different studies (Hovig et al.[17] and Section1), the machine-to-machine repeatability is low. Therefore, surface characterization for the specific machine and material is necessary in order to predict the fatigue life of a LPBF component.

3.2. Porosity

Fig. 4 (left) shows a polished cross-section of an AlSi10Mg cube made with the process parameters used in this study. The porosity content is measured to be 0.50 volume %. The distribution, average diameter, and average circularity of the pores as a function of distance from the edge are shown in Fig. 4 (right). As can be seen in Fig. 4 there is a substantial amount of sub-surface porosity, and the closest distance between the surface and a pore is less than 15 µm. The high concentration of sub-surface porosity is believed to be a result of trapped hydrogen during LPBF processing. The laser first melts the cross section of each cube before finishing with a contour scan along the perimeter. This allows the cross section to solidify before the perimeter is melted, effectively creating a physical barrier which limits the hydrogens ability to diffuse through the outer perimeter during heat treatment. Beevers et al. experimented with AlSi10Mg specimens processed with and without contour scans[19], and found that the largest pores were near the surface in both conditions. The specimen processed with contour scan had the largest pores, but the quantity was higher near the surface when processing without contour scan. However, note that Beevers et al. did not heat treat the specimen.

The measured diameter of the pores ranges from 8 µm to 175 µm, the average pore diameter in each histogram bin range from 15 µm to 42 µm, and the average diameter is 27 µm. The average circularity is 0.88, which indicates that the pores are dominantly spherical.

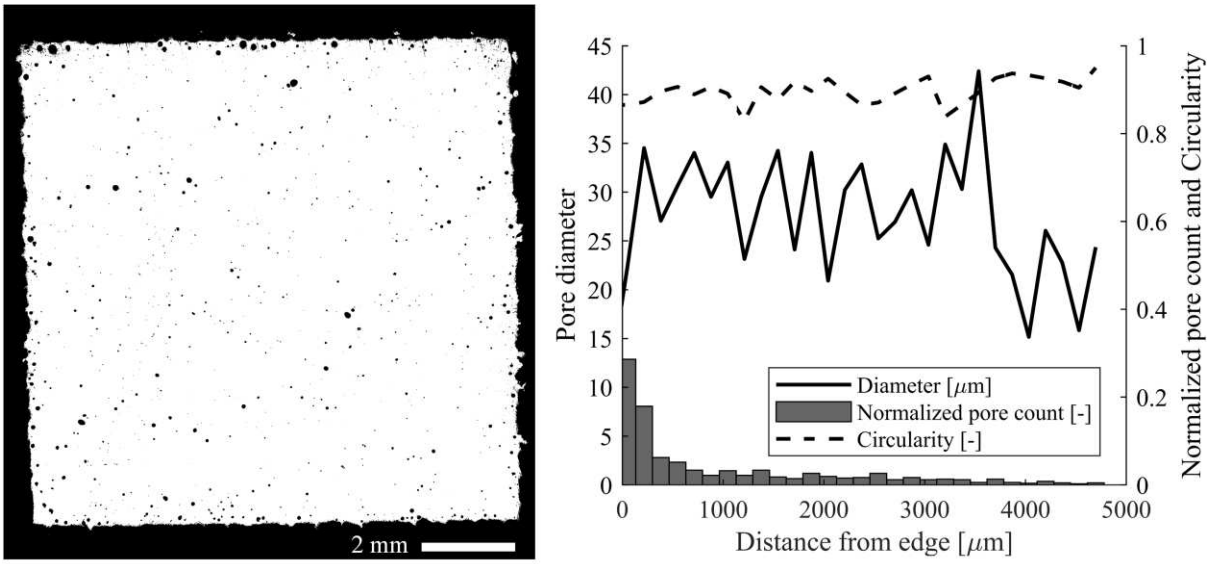

Fig. 4 Optical microscopy image of a cross section of an AlSi10Mg cube cut perpendicular to the build direction (left), and image analysis of the porosity (right).

Fig. 5 shows scanning electron microscope (SEM) micrographs of as-built (Fig. 5 left) and HIP plus aged (Fig. 5 right) Inconel 718. In the as-built condition, two different defects are visible; spherical pores with diameter less than 10 µm, and large irregularly shaped defects with size in the order of 100 µm. The spherical pores are believed to be a result of trapped gas during the processing of feedstock or LPBF sample fabrication[27]. The irregularly shaped defects are attributed to sub-optimal LPBF processing parameters. In the HIP + aged condition the irregularly shaped defects are no longer visible. Some of the smaller pores are retained after HIP + ageing, but the quantity is greatly reduced compared to the as-built

condition. The relative density of the material also increases from 99.97% for the as-built condition to 99.98% for the HIP + aged condition[24].

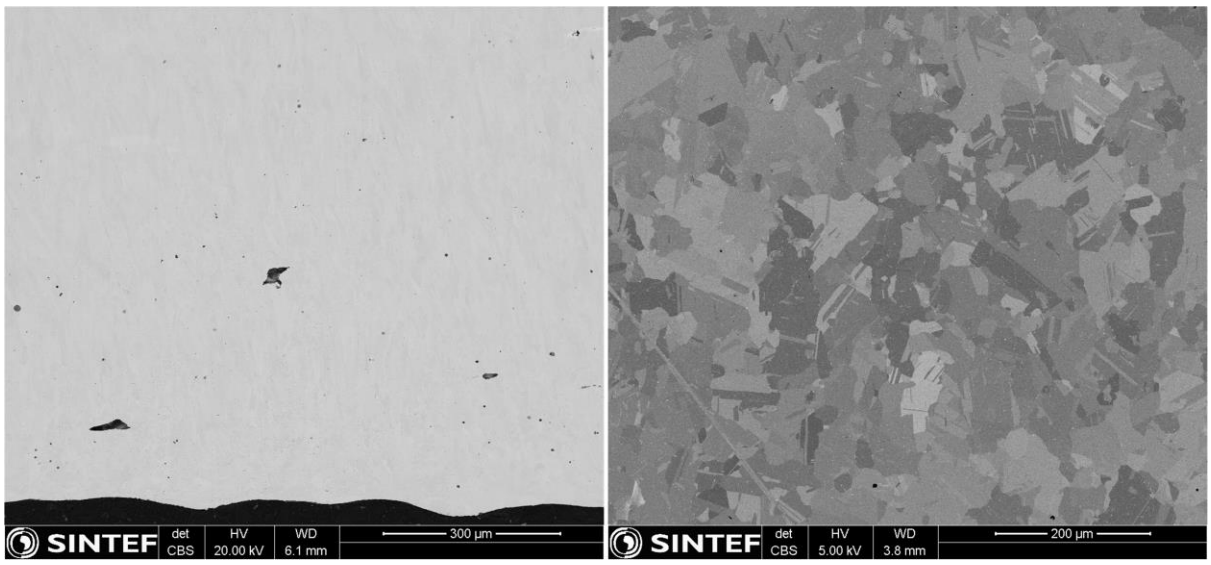

Fig. 5 SEM micrographs of as-built (left), and HIP post-processed (right) Inconel 718 cut perpendicular to the build direction. Note that the scales are different.

In addition to introducing local stress concentrations, the surface defects and the internal defects disrupt the stress distribution around each other. Fig. 6 shows a numerically computed SCF for a generic material, with a U-shaped groove on the surface and a spherical pore close to the groove tip, under uniaxial tensile loading conditions. The pores are assumed spherical since the most defect-prone material in this study (AlSi10Mg) has a circularity close to 1. The upper limit for pore size is chosen based on the observed maximum pore size of AlSi10Mg, and the lower limit set to 50 µm, as the distance where the pore becomes independent of the surface defect is approaching the width of the contour scan (150 µm). As can be seen, both the pore diameter and its distance from the groove tip affect the local stress field. The simulation is carried out with d and ρ selected to give a baseline SCF $k_t = 4.5$, but the general trend would be the same if any other baseline were selected. The SCF increases with increasing pore size and decreasing distance between pore and groove tip. Siddique et al.[28] expressed the SCF of a pore as a function of the pore diameter and distance from the surface (no surface roughness), with values for k_t ranging from 1 to 1.178. When comparing the magnitude of the stress concentration from only surface defects (Eq. 1 and baseline in Fig. 4) and internal pores (Siddique et al.) it becomes clear that SCFs from surface defects are far larger than those from only spherical pores.

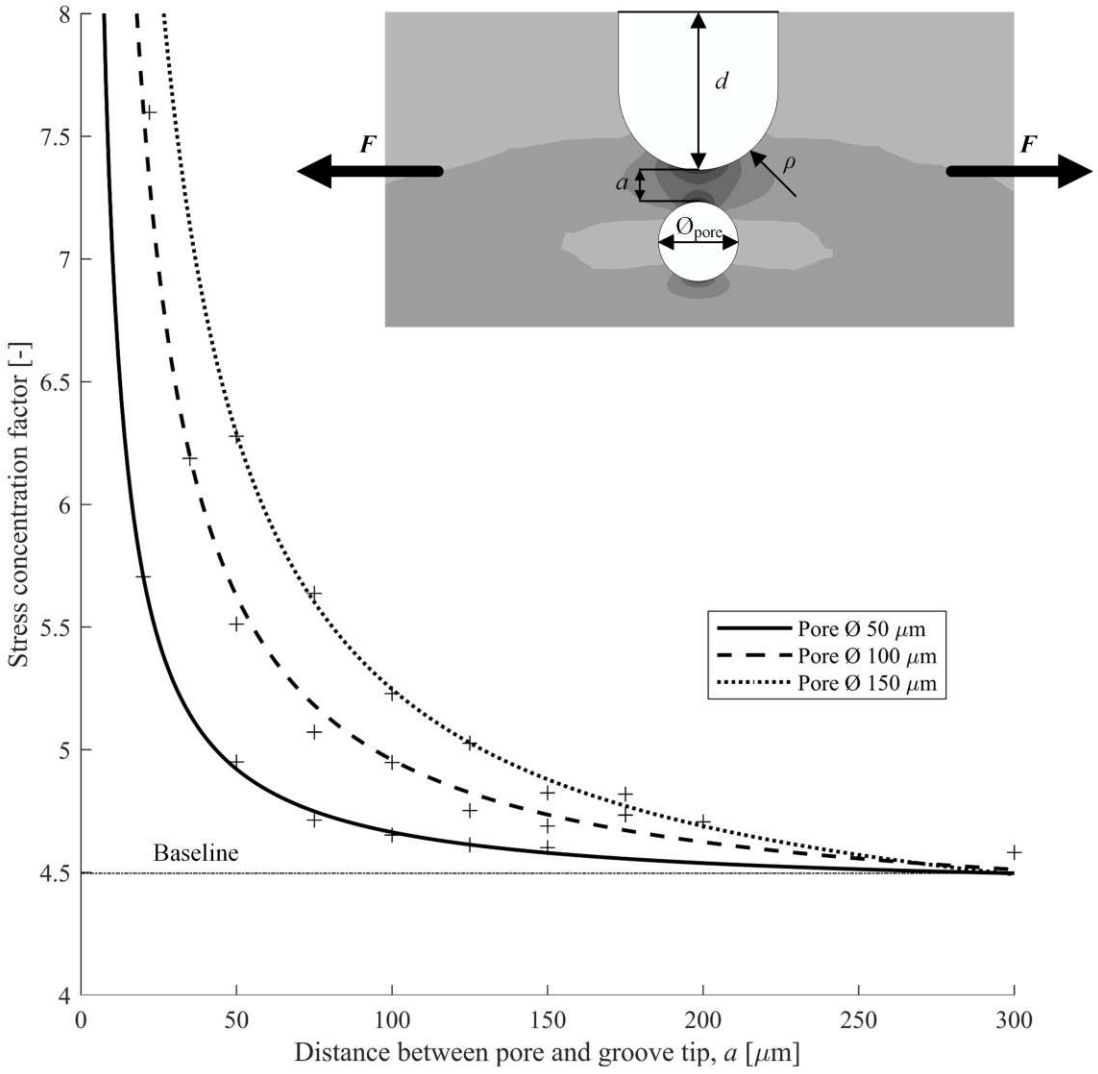

Fig. 6 The effect of pore diameter and distance between pore and crack tip on the SCF of a U-shaped surface defect with nominal SCF of 4.5. The inset shows the relative geometry of the groove and the pore. F indicates the direction of the applied uniaxial tension.

3.3 Stress concentration factors

Consider the simplified schematic of an as-built LPBF surface shown as an inset in Fig. 7. The schematic shows a cross-section of three layers, where the scanning direction alternates with each layer. Each semi-circle represents a single laser track. The hatch spacing is indicated with h, the layer thickness with t, and the inclination angle (of the built part) with θ. The surface can then be considered as a periodic row of laser tracks, where the depth of each valley (between two tracks) is the surface roughness measure R_{vm}. The radius at the depth of the valley, ρ, can be calculated with equation (3);

$$\rho = \frac{L - tan(R_{da})\, R_z}{1 - tan(R_{da})} \tag{3}$$

The width L is the peak-to-peak distance measured as S (mean spacing between adjacent local peaks). The value of R_{da}, R_z, and S may be determined by WLI as in this study, or simply with a perthometer. The SCF for surface defects may then be calculated with equation (2) using R_{vm} as d, and ρ according to equation (3). This method is referred to as the 'stylus method' in the subsequent discussion.

An alternative approach for calculating the SCF of surface defects is to use the mapped topography from WLI. The surface topography is represented in a matrix, with each element, Z_{XY}, corresponding to the height of the pixel indicated by the row (X) and column (Y). The horizontal radius of curvature at each point may then be obtained based on a quadratic fit through that point and the adjacent points. If the data is fit to $\mathrm{Z(X,Y)} = \mathrm{aZ(X,Y)}^2 + \mathrm{bZ(X,Y)} + \mathrm{c}$, the spherical radius of curvature at (X,Y) is approximately $r \cong (2a)^{-1}$. The SCF may then be estimated using equation (2). This method is referred to as the 'WLI method' in the subsequent discussion. The estimated SCFs for the seven specimen orientations were calculated using both the WLI method and the stylus method. The results are shown in Fig. 7 for AlSi10Mg and Fig. 8 for Inconel 718. As expected, the SCF follows the general trend of the surface roughness parameters (Fig. 1, Fig. 2, and Fig. 3).

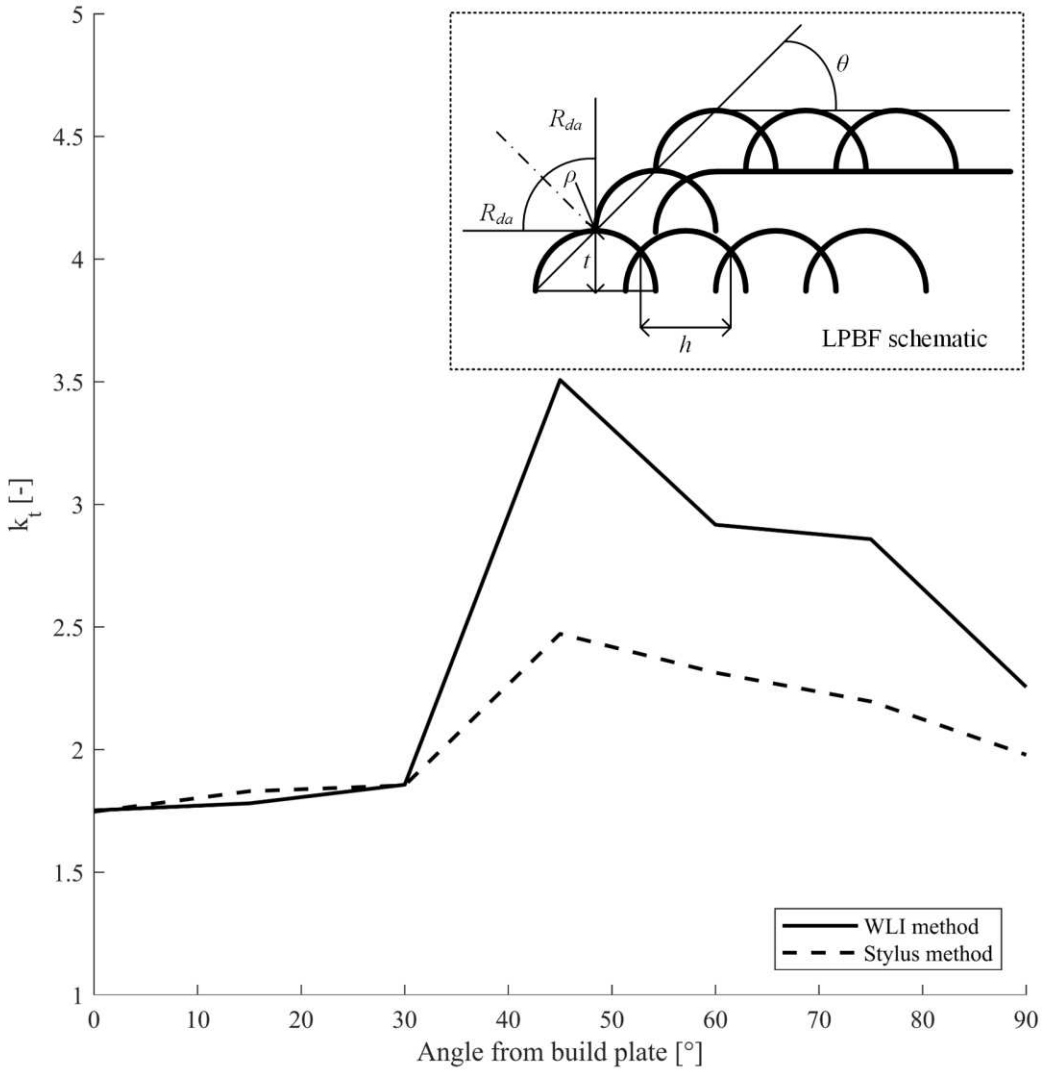

Fig. 7 Estimated SCF for surface defects in AlSi10Mg for all specimen orientations with both the 'WLI method' and the 'stylus method'. The inset is a schematic of three layers of a LPBF process with the relevant parameters for the 'stylus method' indicated.

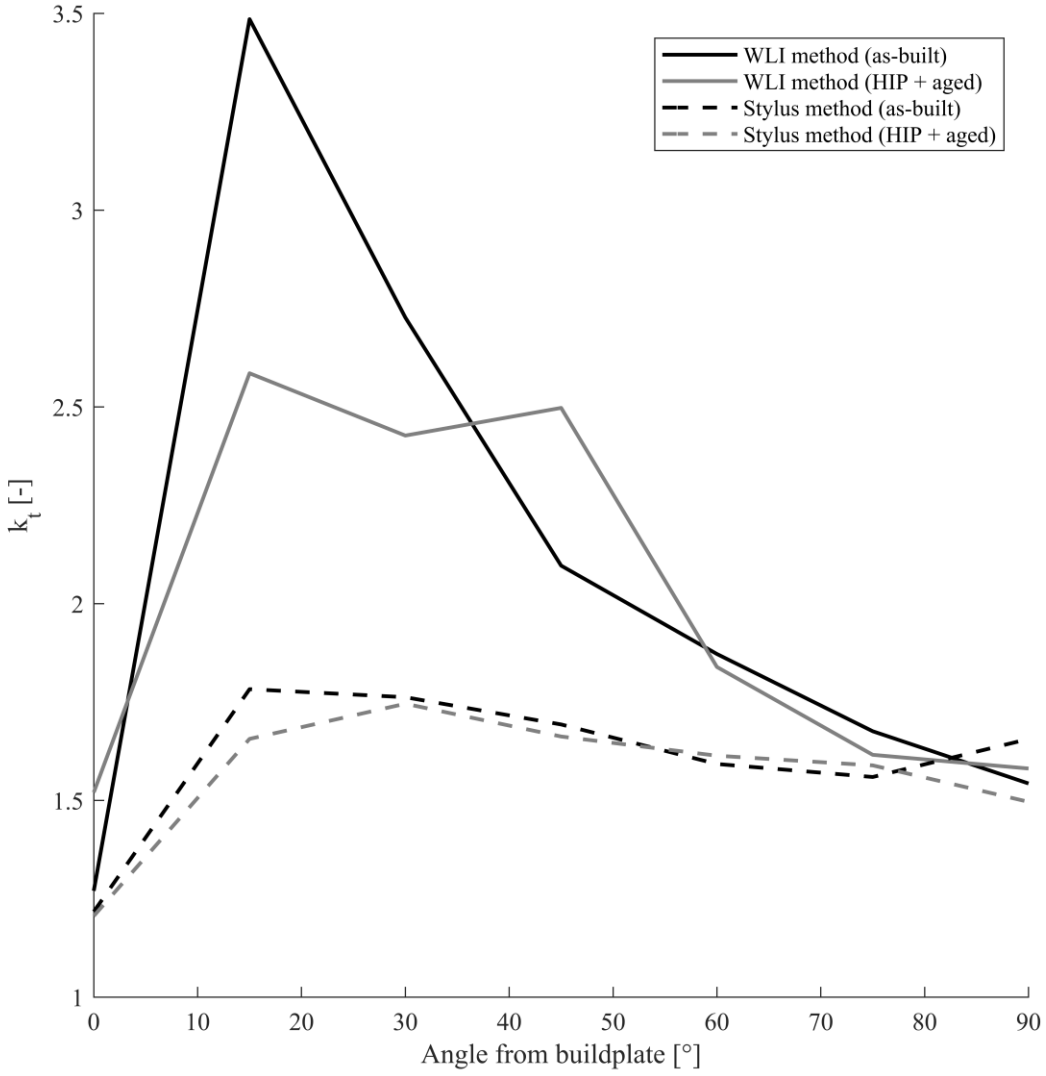

Fig. 8 Estimated SCF for surface defects in Inconel 718 for both heat treatment conditions and all specimen orientations with both the 'WLI method' and the 'stylus method'.

Consider the SCF for AlSi10Mg in Fig. 7. For specimens oriented at angles below 45°, the SCF is relatively low and consistent for both methods. When the surface roughness increases for the specimens oriented at 45° and above, the WLI method gives more conservative values. The stylus method considers either a line on the surface (perthometer), or the average surface roughness of the investigated area (WLI) and averages out the extremities. Consequently, the extremities of the peaks and valleys are given less weight than with the WLI method, resulting in a less conservative estimate of the SCF. For smoother surfaces (0°, 15°, and 30°), the discrepancy between the two methods is relatively small and the estimated SCF is conservative for the stylus method. For rougher surfaces, the WLI method will estimate a more conservative SCF than the stylus method.

In the case of Inconel 718 (Fig. 8) the discrepancy between the WLI method and the stylus method is large across the entire surface inclination range except for surfaces at 0° and 90°. Fig. 9 shows the WLI images of the surface of the horizontal specimens of AlSi10Mg (left), as-built Inconel 718 (middle), and HIP + aged Inconel 718 (right). As can be seen, there is a visible amount of partially fused powder particles on the AlSi10Mg specimen (Fig.9 (left) and Fig.10 (right)), whereas for the horizontal Inconel 718 specimens, there are few if none visible powder particles on the surface. However, when the flat surfaces of the Inconel 718 specimens are built at an angle the partially fused particles appear (Fig. 10 (left)). The presence of particles at the surface will strongly affect the roughness extremes, the base for the WLI method, but it will not alter the average roughness parameters, the base for the stylus method, to the same extent. This can explain the large discrepancies observed between the methods.

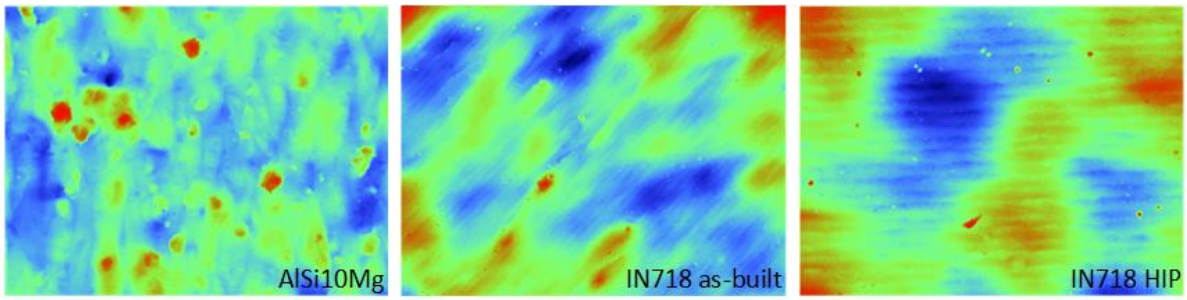

Fig. 9 Un-masked WLI images of the surface of the horizontally oriented specimens of AlSi10Mg (left), as-built Inconel 718 (middle), and HIP + aged Inconel 718 (right). The area investigated is 1.7 mm × 2.3 mm. Red colour indicate high points, while blue indicate low points.

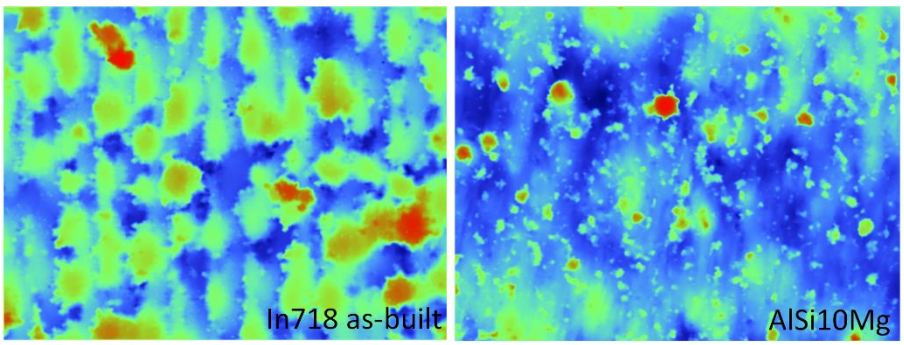

Fig. 10 Un-masked WLI image of the 15° as-built Inconel 718 (left) and the 45° AlSi10Mg (right) specimens. The area investigated is 1.7 *mm* × 2.3 *mm. Red colour indicates high points, while blue indicate low points.*

If the material in question contains sub-surface pores, a modification of the estimated SCFs might be necessary. As shown in Fig. 6 both the pore diameter and the distance between the surface defect and the pore will affect the SCF of the surface defect. If a pore is in close proximity to the surface defect, the local SCF increases, leading to premature crack initiation and reducing the fatigue life. However, as this crack propagates into the pore, the pore will

blunt the crack tip. The effective SCF is then the SCF of the pore. Since the SCFs of pores are in the range of 1 to 1.178[28], further crack propagation will be abated. Statistically speaking, although sub-surface porosity might be present, an ordered distribution of pores which will blunt all cracks is quite unlikely. As a result, the cumulative effect of the surface and sub-surface defects should be considered when designing components subjected to high cycle fatigue loading. Another finding of modelling the crack-pore interaction (Fig. 6) is the distance at which the stress intensity factor becomes independent of pore size and geometry. For the typical range of surface defects, it was found that the pores positioned at 300 µm and farther from the surface defect tip had no effect on the local stress field at the tip. Therefore, in this particular study, sub-surface pores will have to be considered only when they are located closer to the surface than 300 µm.

3.4 High cycle fatigue life estimation

It is widely demonstrated that the specimen build orientation affects the microstructure in terms of texture in Inconel 718 processed by both LPBF[21,22,24,29] and electron beam melting[30]. According to these studies, the variation in the elastic and shear moduli from the weakest to the strongest orientation does not account for more than 10% and 50% respectively. Although for a polished sample with $k_t = 1$ the variation of anisotropic properties is quite influential, these effects are considerably lower than the SCF impact that is shown to amplify the externally applies stress by 150% to 350% ($k_t = 1.5$ to 3.5). Consequently, in the present study, it is considered unnecessary to incorporate the anisotropic properties as the aim is to benchmark the effect of surface roughness on high cycle fatigue life. As a final justification, we would also like to remind the reader that the microstructures of LPBF AlSi10Mg and Inconel 718 undergo extensive recrystallization upon heat treatment and HIPing, respectively, which mitigates the traces of textured microstructure and thus mechanical anisotropy.

In order to demonstrate the effect of surface roughness on high cycle fatigue life, a series of simulations were performed using Abaqus and FE-Safe finite element analysis software. A dog-bone geometry was loaded in tension and compression at 10% of the material's yield strength in Abaqus. Thereafter, it was subjected to a cyclic load in FE-Safe ($R = -1$). The material properties for AlSi10Mg were selected from a study by Hitzler et al.[31] with $E = 62.6$ GPa, $\nu = 0.30$, and $\sigma_y = 198$ MPa. The model is based on an experimentally determined SN curve, and the fatigue life is calculated for the different stress concentration factors measured for the various surface conditions. As a reference SN curve for LPBF AlSi10Mg in T6 condition, the fit from the machined T6 condition in Hovig et al.[17] was used. For aged

Inconel 718 the material properties were determined in a preceding study by the current authors[24], with E = 181 GPa, ν = 0.40 and σ_y = 1085 MPa. For aged Inconel 718, published data for machined and aged Inconel 718[23] was used.

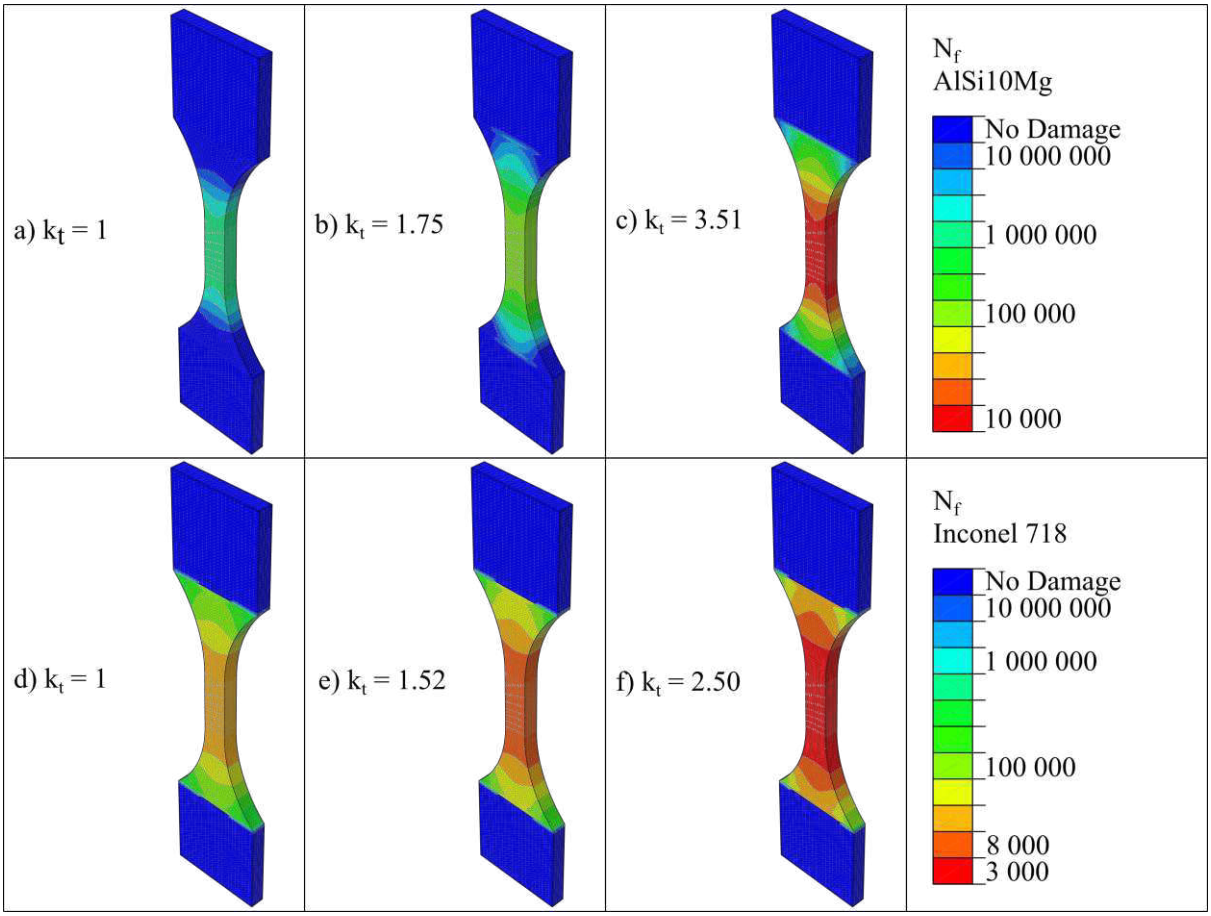

Fig. 11 Fatigue life simulations of AlSi10Mg and Inconel 718 with different surface conditions. (a – c) show AlSi10Mg with SCF values according to polished surface, horizontal orientation, and 45° orientation, respectively. (d – f) show the same for Inconel 718. The legend shows expected number of cycles to failure, N_f. The SCFs were selected from the WLI method.

According to Fig. 11, the fatigue lifetime is reduced by approximately two orders of magnitude for AlSi10Mg and one order of magnitude for Inconel 718, when the specimen build inclination changes from horizontal to 45˚. Since the processing parameters and scanning strategy for these two alloys were different, it can be inferred that changing the process parameters may also influence the fatigue lifetime of the material. The island scanning strategy that was used for AlSi10Mg seems to have an unfavourable effect on the surface properties, although this must be checked by comparing the two processing methods with the same material and powder. When comparing the resulting surface roughness of LPBF Inconel 718 in this work and previously published studies[21,22] (R_a in the order of 5-17 µm depending on orientation) with published values for surface roughness for AlSi10Mg[12,14,18] (R_a in the order of 10-24 µm depending on orientation) it is apparent that the

Inconel 718 alloy generally has a lower surface roughness. Thus, implementing the scan strategy used on the Inconel 718 specimens on the AlSi10Mg specimens does not guarantee comparable surface finishes. In a recent study by Witkin et al.[32], notched fatigue specimens of LPBF Inconel 718 were tested with as-built and machined surfaces. The machined and notched specimens with the highest nominal SCF (k_t = 3.10) had a longer fatigue life than as-built (un-notched) specimens with nominal SCFs of k_t = 2.00 and k_t = 2.24. The results from Witkin et al. implies that even when notched defects with SCFs of three times that of a polished un-notched surface are introduced, the surface roughness is still the dominating effect when it comes to defect induced fatigue life reduction.

In general the fatigue lives reported here, calculated using equation (2), are based on SCFs due to uniaxial tension. This should be considered the worst-case loading scenario[2], and gives the most conservative estimate.

4 Conclusions

This study presents two methods for estimating stress concentration factors for high cycle fatigue life prediction of AlSi10Mg and Inconel 718 processed by laser powder bed fusion (LPBF). The methods are based on surface roughness data as input. Compared to the 'WLI method', the 'stylus method' estimates a longer fatigue life for rough surfaces. For smoother surfaces the difference between the methods is small.

In porosity free materials, the stress concentration factor, and thus the high cycle fatigue life, is a function of the surface roughness. HIP + ageing was shown to be effective in reducing the surface roughness and the quantity of internal defects in Inconel 718. Consequently, the stress concentration factor will be reduced. In the case of AlSi10Mg, sub-surface defects are present, and their effect must be considered through the methods proposed by e.g. Romano et al.[4], Yamashita et al.[7], or as a multiplier to the SCF based on the worst-case scenario acquired from the surface roughness, average pore size, and distance from the surface anomalies (see Fig. 6).

Based on the investigated model in this work, the stress concentration factor of a surface defect is affected by internal defects if the diameter of the internal defect is sufficiently large, and the distance between the surface defect and the internal defect is sufficiently small. Although the maximum stress at the surface defect increases, a resulting crack will be blunted

when it propagates into the internal defect. Thus, a more comprehensive model is necessary in order to estimate the fatigue life of components with sub-surface defects.

Acknowledgements

The authors acknowledge funding from the Research Council of Norway (grant no. 248243, the MKRAM project) and SINTEF's strategic project on additive manufacturing, SIP-LAMINA. Inconel 718 specimens were provided by Promet AS, 4056 Tananger, Norway. Heat treatment of Inconel 718 specimens were performed by Bodycote AB, 735 31 Surahammar, Sweden. The authors certify that they have no conflict of interest in the subject matter or materials discussed in this manuscript.

References

1 Yap, C., Chua, C., Dong, Z., Liu, Z., Zhang, D., Loh, L. *et al.* Review of selective laser melting: Materials and applications. *Appl. Phys. Rev.* 2015; 2:

2 Pilkey, W. D. & Pilkey, D. F. *Peterson's stress concentration factors*. Hoboken, NJ, USA: John Wiley; 2008.

3 Siddique, S., Awd, M., Tenkamp, J. & Walther, F. Development of a stochastic approach for fatigue life prediction of AlSi12 alloy processed by selective laser melting. *Eng. Fail. Anal.* 2017; 79: 34-50.

4 Romano, S., Brückner-Foit, A., Brandão, A., Gumpinger, J., Ghidini, T. & Beretta, S. Fatigue properties of AlSi10Mg obtained by additive manufacturing: Defect-based modelling and prediction of fatigue strength. *Eng. Fract. Mech.* 2018; 187: 165-189.

5 Romano, S., Patriarca, L., Foletti, S. & Beretta, S. LCF behaviour and a comprehensive life prediction model for AlSi10Mg obtained by SLM. *Int. J. Fatigue*. 2018; 117: 47-62.

6 Yadollahi, A., Mahtabi, M. J., Khalili, A., Doude, H. R. & Newman, J. C. Fatigue life prediction of additively manufactured material: Effects of surface roughness, defect size, and shape. *Fatigue Fract. Eng. M.* 2018; 41: 1602-1614.

7 Yamashita, Y., Murakami, T., Mihara, R., Okada, M. & Murakami, Y. Defect analysis and fatigue design basis for Ni-based superalloy 718 manufactured by selective laser melting. *Int. J. Fatigue*. 2018; 117: 485-495.

8 Zhou, Z., Xu, H., Li, C. & Chen, G. The effect of texture on the low cycle fatigue property of Inconel 718 by selective laser melting. *MATEC Web Conf.* 2018; 165:

9 Aydinöz, M. E., Brenne, F., Schaper, M., Schaak, C., Tillmann, W., Nellesen, J. *et al.* On the microstructural and mechanical properties of post-treated additively manufactured Inconel 718 superalloy under quasi-static and cyclic loading. *Mater. Sci. Eng., A*. 2016; 669: 246-258.

10 Chlebus, E., Gruber, K., Kuźnicka, B., Kurzac, J. & Kurzynowski, T. Effect of heat treatment on the microstructure and mechanical properties of Inconel 718 processed by selective laser melting. *Mater. Sci. Eng., A*. 2015; 639: 647-655.

11 Ni, M., Chen, C., Wang, X., Wang, P., Li, R., Zhang, X. *et al.* Anisotropic tensile behavior of in situ precipitation strengthened Inconel 718 fabricated by additive manufacturing. *Mater. Sci. Eng., A*. 2017; 701: 344-351.

12 Aboulkhair, N. T., Maskery, I., Tuck, C., Ashcroft, I. & Everitt, N. M. Improving the fatigue behaviour of a selectively laser melted aluminium alloy: Influence of heat treatment and surface quality. *Mater. Des.* 2016; 104: 174-182.

13 Brandl, E., Heckenberger, U., Holzinger, V. & Buchbinder, D. Additive manufactured AlSi10Mg samples using Selective Laser Melting (SLM): Microstructure, high cycle fatigue, and fracture behavior. *Mater. Des.* 2012; 34: 159-169.

14 Maskery, I., Aboulkhair, N., Tuck, C., Wildman, R., Ashcroft, I., Everitt, N. *et al.* Fatigue performance enhancement of selectively laser melted aluminium alloy by heat treatment. In: eds. *Proceedings of 26th Annual International Solid Freeform Fabrication Symposium.* Austin, Texas, USA: 2015:1017-1025.

15 Mower, T. M. & Long, M. J. Mechanical behavior of additive manufactured, powder-bed laser-fused materials. *Mater. Sci. Eng., A*. 2016; 651: 198-213.

16 Siddique, S., Imran, M. & Walther, F. Very high cycle fatigue and fatigue crack propagation behavior of selective laser melted AlSi12 alloy. *Int. J. Fatigue*. 2017; 94: 246-254.

17 Hovig Even, W., Azar Amin, S., Sunding Martin, F., Sørby, K., M'Hamdi, M. & Andreassen, E. High cycle fatigue life estimation of AlSi10Mg processed by laser powder bed fusion. *MATEC Web Conf.* 2018; 188:
18 Bagherifard, S., Beretta, N., Monti, S., Riccio, M., Bandini, M. & Guagliano, M. On the fatigue strength enhancement of additive manufactured AlSi10Mg parts by mechanical and thermal post-processing. *Mater. Des.* 2018; 145: 28-41.
19 Beevers, E., BrandãO, A. D., Gumpinger, J., Gschweitl, M., Seyfert, C., Hofbauer, P. *et al.* Fatigue properties and material characteristics of additively manufactured AlSi10Mg – Effect of the contour parameter on the microstructure, density, residual stress, roughness and mechanical properties. *Int. J. Fatigue*. 2018; 117: 148-162.
20 Scott-Emuakpor, O., George, T., Holycross, C., Bruns, J. & Zearley, A. Bending Fatigue Life Comparison between DMLS and Cold-rolled Nickel Alloy 718. In: eds. *Proceedings of* Virginia Beach, Virginia, USA: 2014:
21 Kelley, P. F., Saigal, A., Vlahakis, J. K. & Carter, A. Tensile and Fatigue Behavior of Direct Metal Laser Sintered (DMLS) Inconel 718. In: eds. *Proceedings of* Houston, Texas, USA: American Society of Mechanical Engineers; 2015:
22 Konečná, R., Nicoletto, G., Kunz, L. & Bača, A. Microstructure and directional fatigue behavior of Inconel 718 produced by selective laser melting. In: eds. *Proceedings of* Catania, Italy: 2016:2381-2388.
23 Balachandramurthi, A. R., Moverare, J., Dixit, N. & Pederson, R. Influence of defects and as-built surface roughness on fatigue properties of additively manufactured Alloy 718. *Mater. Sci. Eng. A*. 2018; 735: 463-474.
24 Hovig, E. W., Azar, A. S., Grytten, F., Sørby, K. & Andreassen, E. Determination of Anisotropic Mechanical Properties for Materials Processed by Laser Powder Bed Fusion. *Adv. Mater. Sci. Eng.* 2018; 2018:
25 Boschetto, A., Bottini, L. & Veniali, F. Roughness modeling of AlSi10Mg parts fabricated by selective laser melting. *J. Mater. Process. Technol.* 2017; 241: 154-163.
26 Strano, G., Hao, L., Everson, R. M. & Evans, K. E. Surface roughness analysis, modelling and prediction in selective laser melting. *J. Mater. Process. Technol.* 2013; 213: 589-597.
27 Aboulkhair, N. T., Everitt, N. M., Ashcroft, I. & Tuck, C. Reducing porosity in AlSi10Mg parts processed by selective laser melting. *Addit. Manuf.* 2014; 1-4: 77-86.
28 Siddique, S., Imran, M., Rauer, M., Kaloudis, M., Wycisk, E., Emmelmann, C. *et al.* Computed tomography for characterization of fatigue performance of selective laser melted parts. *Mater. Des.* 2015; 83: 661-669.
29 Gribbin, S., Bicknell, J., Jorgensen, L., Tsukrov, I. & Knezevic, M. Low cycle fatigue behavior of direct metal laser sintered Inconel alloy 718. *Int. J. Fatigue*. 2016; 93: 156-167.
30 Kirka, M. M., Greeley, D., Hawkins, C. & Dehoff, R. Effect of anisotropy and texture on the low cycle fatigue behavior of Inconel 718 processed via electron beam melting. *Int. J. Fatigue*. 2017; 105: 235-243.
31 Hitzler, L., Janousch, C., Schanz, J., Merkel, M., Heine, B., Mack, F. *et al.* Direction and location dependency of selective laser melted AlSi10Mg specimens. *J. Mater. Process. Technol.* 2017; 243: 48-61.
32 Witkin, D. B., Patel, D. N. & Bean, G. E. Notched fatigue testing of Inconel 718 prepared by selective laser melting. *Fatigue Fract. Eng. M.* 2018; 42: 166-177.